

Generalized stacking faults energies of face-centered cubic high-entropy alloys: A first-principles study

Xiaojie Li ^{a,b,*}, Stephan Schönecker ^b, Levente Vitos ^{b,c,d}, Xiaoqing Li ^{b,**}

^a Department of Physics, Taizhou University, Taizhou, 318000, Zhejiang, China

^b Department of Materials Science and Engineering, KTH Royal Institute of Technology, Stockholm, SE-10044, Sweden

^c Research Institute for Solid State Physics and Optics, Wigner Research Center for Physics, Budapest, H-1525, P.O. Box 49, Hungary

^d Department of Physics and Astronomy, Division of Materials Theory, Uppsala University, Box 516, SE-75120, Uppsala, Sweden

ARTICLE INFO

Keywords:

Generalized stacking faults energies
Face-centered cubic
High-entropy alloys
Twinnability
Martensitic transformation

ABSTRACT

Developing high-strength and ductile face-centered cubic (fcc) high-entropy alloys (HEAs) has attracted significant attention. The generalized stacking fault energy (GSFE) is a very useful concept to describe stable and unstable planar defects and their energies on a slip plane. It plays an essential role in designing high performance fcc HEAs and understanding the nanoscale plasticity phenomena. In this work, using first-principles simulations, we investigate the configuration-averaged GSFEs of 29 single-phase fcc HEAs and identify indicators that can be used to tune stacking fault energies. First we determine the equilibrium structural parameters for all considered alloys and compare them with available experimental data. With the obtained GSFEs, we analyze the relationship between the stacking fault energies and materials properties, and investigate scaling relations between planar fault energies and the tendencies to exhibit deformation twinning and transformation to hexagonal close-packed martensite. We find that unstable SFE and shear modulus correlates strongly. Moreover, we reveal that the ratio of intrinsic SFE to unstable SFE, $\gamma_{isf}/\gamma_{usf}$, is a characteristic materials measure, and the tendencies to twinning and martensitic transformation rank with it. Our results are expected to be useful for an efficient alloy design and selection of solutes in fcc HEAs.

1. Introduction

Research in high-entropy alloys (HEAs) has attracted significant attention in material science and engineering following the publications of Yeh *et al.* [1] and Cantor *et al.* [2] in 2004. Many HEAs synthesized so far form solid solution phases with simple structures including the face-centered cubic (fcc) structure and body-centered cubic structure. An important goal for fcc HEAs is to develop new compositions that exhibit a combination of high strength and good ductility. Tailoring plastic deformation mechanisms has been proven to be one of the most promising routes to achieve increases in strain hardening and ductility, in particular design approaches based on metastability including transformation-induced plasticity and twinning-induced plasticity

effects [3].

Slip, deformation twinning, and transformation to hexagonal close-packed (hcp) martensite are dislocation-mediated, competing plastic deformation modes in many fcc metals and alloys. The predominantly active mode is often claimed to be correlated with the value of intrinsic stacking fault energy (ISFE) [4,5]. Deformation twinning, for instance, is characteristic of fcc materials with low to medium ISFE. However, the ISFE alone does not provide a complete picture of the prevailing plastic deformation mode. For instance, both Ag and Ir twin under ordinary loading conditions at room temperature [6–9], but have low ISFE (16 mJ/m^2) and high ISFE (480 mJ/m^2), respectively [10,11].

The generalized stacking fault energy (GSFE) [12] is an important theoretical concept to understand structure and energetics of

Abbreviations: HEA, high-entropy alloy; ISFE, intrinsic stacking fault energy; fcc, face-centered cubic; hcp, hexagonal close-packed; GSFE, generalized stacking fault energy; ISF, intrinsic stacking fault; USF, unstable stacking fault; CPA, coherent-potential approximation; CRSO, chemical short-range order; EMTO, exact muffin-tin orbitals; SF, stacking fault; TW, twinning; SL, full slip; NP, nano-hcp phase; UTF, unstable twin fault; UPF, unstable phase fault; DFT, density-functional theory.

* Corresponding author. Department of Physics, Taizhou University, Taizhou, 318000, Zhejiang, China.

** Corresponding author.

E-mail addresses: lixj26@tzc.edu.cn (X. Li), xiaoqli@kth.se (X. Li).

<https://doi.org/10.1016/j.intemet.2022.107556>

Received 5 December 2021; Received in revised form 21 March 2022; Accepted 26 March 2022

Available online 1 April 2022

0966-9795/© 2022 Elsevier Ltd. All rights reserved.

dislocation-mediated slip processes in metals and alloys including ductility [13], twin nucleation mechanisms and stresses [14], competing plastic deformation mechanisms [15–17], and solid-solution strengthening [18]. The conventional GSFE $\gamma(x)$ measures the energy excess for alias shearing two adjacent lattice planes relative to each other along a , in general, discontinuous slip path [19],

$$\gamma(x) = [E(x) - E(0)]/A, \quad (1)$$

where $E(x)$ is the energy of the sheared lattice relative to that of the defect-free one $E(0)$. The excess energy is normalized to the cross-sectional area A , and x is the shear displacement projected onto the slip path. The extrema of GSFE curves correspond to stable and unstable planar faults energies, and energy barriers derived from the curves provide a measure of the resistance to produce stable faults along the slip path. We focus here on the usual $[10\bar{1}](111)/2$ slip systems in the fcc phase, where perfect dislocations dissociate into partials which length of the Burgers vector is b_p . The unstable stacking fault (USF) energy γ_{usf} measures the resistance to create an intrinsic stacking fault (ISF) with energy γ_{isf} in a defect-free fcc lattice, see Fig. 1.

There are established, although challenging, experimental methods to estimate the excess energy of some stable planar faults, for instance γ_{isf} via the equilibrium separation of partial dislocations bounding the ISF, but unstable planar faults energies have largely proved elusive for measurements so far. In regard to γ_{isf} , theory and experiment tend to agree in fcc materials with $\gamma_{isf} > 0$, while discrepancies occur in metastable fcc materials where calculations predict $\gamma_{isf} < 0$. While Xun *et al.* suggested that models interpreting results of current experimental methods are biased towards positive values of the ISFE [20], Werner *et al.* recently proposed a correction to the “apparent” positive, experimental ISFEs, which would allow validation of negative values of the ISFE in metastable fcc materials [21]. All in all, first-principles calculations and atomistic simulations are the primary tools to obtain GSFEs.

In this work, we focus on a series of 29 transition metal HEAs, which were previously synthesized in the fcc phase and, in the cases where their microstructure was examined, displayed transformation-induced plasticity or twinning induced plasticity effects. A detailed knowledge on the fundamental deformation mechanisms underlying their crystal plasticity are, in most cases, lacking. The present work provides information on equilibrium properties from first-principles investigations, analyses indicators that can be used to tune the stable and unstable

stacking fault energies, and discusses plastic deformation modes. Thirteen of the 29 alloys possess low but positive ISFEs ($0 \leq \gamma_{isf} \leq 39 \text{ mJ/m}^2$), and the remaining 16 alloys have negative ISFEs. This suggests that the fcc phase in the latter set is metastable as the energy difference between the hcp and fcc phases scales with γ_{isf} [22]. The present results are expected to help the alloy design and provide a selection of solutes in stable and metastable fcc HEAs.

2. Theory and method

To calculate intrinsic materials properties of HEAs, we employed density-functional theory (DFT) [23] and the Perdew-Burke-Ernzerhof generalized-gradient approximation [24]. The Kohn-Sham equations [25] were solved with the Exact Muffin-Tin Orbitals (EMTO) method and full charge-density technique [26,27] including s, p, d, and f orbitals in the basis set. The electronic structure of substitutionally disordered HEAs was treated with the coherent-potential approximation (CPA) [28] as implemented in EMTO [29]. The CPA determines an effective medium, whose properties are as close as possible to those of the configuration average of a disordered alloy, by demanding that a single atom of the alloy components embedded in the effective medium does not change its scattering properties on the concentration average. As the CPA neglects non-local correlations beyond the single site, it can not describe statistically correlated ensembles associated with, e.g., chemical short-range order (CSRO). Further, local lattice relaxations can not directly be treated by the CPA. All our calculations assumed the paramagnetic (PM) state, which was described by the random alloy analogue of the disordered-local moment model [30]. We chose the PM state as the Curie temperatures estimated from the mean field approximation [30,31] are below room temperature (except CoCrFeNiPd) consistent with the available experimental data [32–38]. After careful testing, we performed Brillouin zone integrations with 20×10^3 to 25×10^3 uniformly distributed k -points in the elastic constants calculations and with $12 \times 24 \times 3$ k -points meshes in the GSFE calculations.

The GSFE surfaces were determined using tilted supercells [39] composed of nine (111) fcc layers and applied simple alias shear as described in detail in Ref. [40]. The three independent single-crystal elastic constants for the fcc structure, C_{11} , C_{12} , and C_{44} , were obtained by applying volume-conserving strains to the fcc structure in mechanical equilibrium and least-square fitting the recorded energy-strain relationships; see our previous work for all necessary details [29]. Based

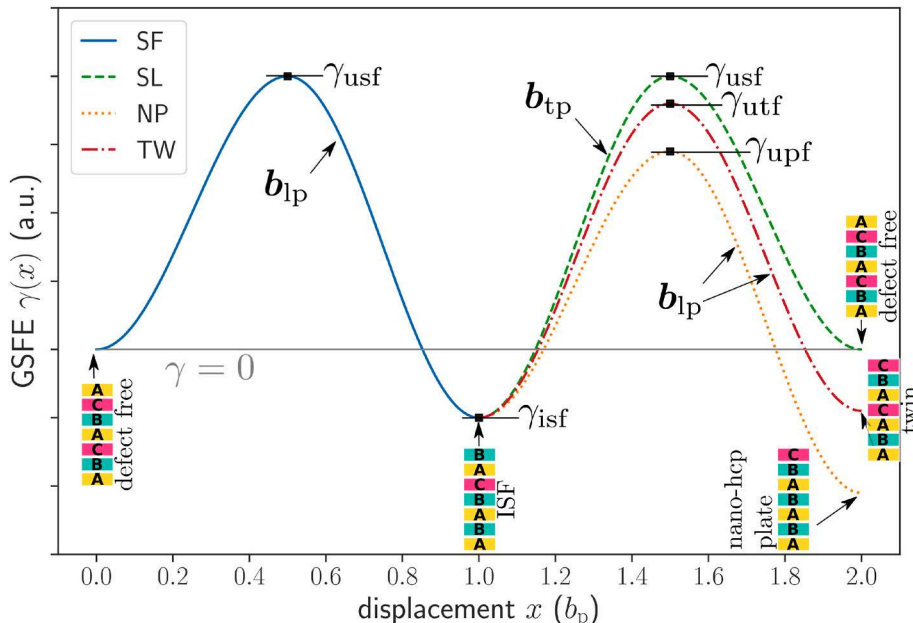


Fig. 1. Schematic GSFE curves $\gamma(x)$ for $[11\bar{2}]$ alias shear on (111) planes in a metastable fcc crystal. The displacement x is projected onto the slip path and in units of the magnitude of partial Burgers vector (b_p). Displacements 0–1 b_p (blue solid line, SF mode) result in an ISF with energy γ_{isf} . Displacements 1–2 b_p result in either a twin fault (red dash-dotted line, TW mode), a nano-hcp plate (orange dotted line, NP mode), or complete the full slip (green dashed line, SL mode). These slip processes may be interpreted in terms of nucleation of leading b_{lp} and trailing b_{tp} partials as described in the main text, where also the unstable stacking energies are defined. The (111) stacking sequences of the perfect lattice and the various stable planar defects are indicated, in which the three colors with block letter A, B, C correspond to the three possible atomic positions in a (111) close-packed plane.

on the C_{ij} , we estimated the effective shear modulus G and Young's modulus E of poly-crystalline, statistically isotropic and homogeneous aggregates using Voigt-Reuss-Hill averaging [41], $G = 1/2(G_R + G_V)$, where

$$G_R = \frac{5(C_{11} - C_{12})C_{44}}{4C_{44} + 3(C_{11} - C_{12})} \quad (2)$$

$$G_V = \frac{C_{11} - C_{12} + 3C_{44}}{5}. \quad (3)$$

E is related to G and the bulk modulus B through

$$E = \frac{9BG}{3B + G}. \quad (4)$$

We used a Morse equation of state [42] to determine the bulk modulus as well as the equilibrium lattice parameter a .

The accuracy of the EMTO-CPA method for the equation of states, elastic properties, and stacking fault energies of alloys has been demonstrated in a number of previous works [40,43–45].

3. Results and discussions

The calculated materials parameters for the 29 considered fcc HEAs, i.e., lattice parameters, elastic constants, various stable and unstable planar defect energies, are listed in Table 1 and discussed in the following.

The available room-temperature experimental lattice parameters shown in Table 1 agree well with the present theoretical values (largest absolute deviation is 1.7%). Evaluation of the Born stability criteria [59] suggests that the fcc phase is elastically stable at zero temperature and pressure in all the alloys, which is consistent with the experimental observation at room temperature.

Fig. 2(a) shows a strong linear correlation between the Young's modulus and shear modulus in the HEAs, in which the theoretical ratio $E/G \approx 2.59$ obtained using a linear regression function with zero

intercept is close to the ratio of 2.56 observed for polycrystals of conventional fcc elements and alloys [60].

A useful evaluation of our results for γ_{ISF} comes from an assessment of them in relation to the shear elastic constant C_{44} . Fig. 2(b) shows a nonlinear relationship between the ISFEs and the values of C_{44} . A least-squares fit with an exponential function $\gamma_{\text{ISF}} = c_1 \exp(c_2 C_{44}) + c_0$, c_0 , c_1 and c_2 being coefficients, has a coefficient of determination $R^2 = 0.8$. Overall, this correlation indicates that the single-crystal shear elastic constant C_{44} may be used to tailor the ISFE.

We reiterate that the present GSFE probes the total energy landscape for alias shear strains involving pairs of adjacent (111) planes displaced in the $[11\bar{2}]$ direction. In contrast, the shear modulus is concerned with the strain energy due to (infinitesimally) small affine shear involving every lattice plane parallel to which shear is applied. To examine a possible correlation between material properties characteristic for these shear types in the limit of vanishing strain, we consider the modulus for shear on the (111) plane in the $[11\bar{2}]$ direction, $G^{\text{res}} = (C_{11} - C_{12} + C_{44})/3$. To describe the small-strain behavior of the GSFE, we approximate it by a standard expression $\gamma(x) = \gamma_{\text{usf}} \sin^2(\pi x/b_p)$ in the interval $0 \leq x/b_p \leq 0.5$. By definition, $\gamma_{\text{usf}} \equiv \gamma(x = 0.5)$. For the second order derivative of $\gamma(x)$ with respect to x at vanishing displacement follows $d^2\gamma(x)/dx^2|_{x=0} = 2\gamma_{\text{usf}}(\pi/b_p)^2 \alpha \gamma_{\text{usf}}$. To put the correlation to the test, Fig. 2(c) plots the calculated γ_{usf} versus $G^{\text{res}} \Omega^{1/3}$, where the equilibrium volume per atom Ω is used to convert to units of J/m^2 . This exercise reveals that γ_{usf} and $G^{\text{res}} \Omega^{1/3}$ are strongly correlated. Assuming a linear regression function of the form $\gamma_{\text{usf}} = c_1 G^{\text{res}} \Omega^{1/3} + c_0$, we determined a coefficient of determination $R^2 = 0.97$.

The correlation between the USFE and the resolved shear modulus may be of limited practical usefulness for metallurgists as the evaluation of G^{res} requires knowledge of all the single-crystal elastic constants. On the other hand, the polycrystal shear modulus is easily attainable experimentally, e.g., through ultrasound methods. Fig. 2(d) shows a strong linear correlation between γ_{usf} and G . The coefficient of determination $R^2 = 0.96$ assuming a similar linear regression function as

Table 1

Listed are the calculated lattice parameters, elastic constants (in GPa), unstable stacking fault energy (USFE), intrinsic stacking fault energy (ISFE), unstable twinning fault energy (UTFE), and unstable phase fault energy (UPFE; all in mJ/m^2) for the considered fcc HEAs. Available experimental lattice parameters are listed in parentheses.

HEAs	a (Å)	C_{11}	C_{12}	C_{44}	USFE	ISFE	UTFE	UPFE
CoCr2.5Fe2Mn0.5Ni4 [46]	3.540	255.5	176.9	163.1	319.8	-4.0	312.2	310.8
Co2Cr2.5FeMn0.5Ni4 [46]	3.533	270.0	182.8	168.9	333.4	-4.6	325.2	323.8
VCrFe4.5Co3.5 [47]	3.529 (3.592)	256.7	161.2	179.8	326.6	-115.5	275.4	208.7
CoCrFeNi [48]	3.527	270.5	178.6	175.2	336.1	-39.7	311.8	292.4
CoCrMnNi [49]	3.532	253.6	165.3	174.8	324.7	-84.8	283.0	236.8
Co2CrCuFeMnNi [50]	3.548 (3.568)	237.1	156.6	162.2	325.9	13.9	326.4	333.5
CoCrNiW0.01 [51]	3.530 (3.579)	288.3	196.8	174.5	336.6	-39.9	312.1	292.3
CuNi2FeMn2Cr [52]	3.580 (3.611)	187.5	130.9	142.0	287.0	39.1	301.3	321.7
CuNiCoFeCrTi [33]	3.638	177.8	155.2	115.1	198.2	16.1	205.0	214.3
CuNiCoFeCrTi0.5 [33]	3.600	200.4	156.5	130.8	248.4	19.2	254.7	265.0
CuNiFeCrMo [53]	3.711	174.4	153.9	113.9	215.5	9.8	220.4	224.9
FeCoNiCrCu [53]	3.557	236.3	168.2	150.8	306.9	32.2	316.6	332.9
FeCrMnNiCo [45]	3.527	249.2	156.1	178.9	331.2	-95.4	285.1	232.5
CoCrCuFeMnNi [50]	3.563 (3.572)	217.0	149.8	152.0	303.8	20.2	308.4	319.2
CoCrFeNiPd [54]	3.662 (3.670)	209.4	130.6	144.6	318.1	31.9	328.9	345.2
Co2CrFe5NiV [55]	3.540	238.6	158.0	168.2	307.8	-66.1	277.5	239.6
CoCrFeMn0.25Ni2Zn0.75 [35]	3.577 (3.589)	217.2	163.4	141.5	257.6	30.1	270.1	283.7
CoCrCu0.5FeNi [56]	3.544 (3.562)	248.7	171.3	161.1	319.5	8.3	317.3	322.6
Co1.5CrCuFeMnNi [50]	3.555 (3.571)	224.8	150.6	157.1	315.1	16.7	317.5	326.2
FeCrCoNiMo0.23 [57]	3.570	252.6	176.3	161.3	304.1	-49.5	279.0	253.3
NiCoFeCrMo0.3 [57]	3.581	252.6	180.3	158.1	296.0	-51.4	270.7	243.8
VCrFe4.5CoNi2.5 [47]	3.551 (3.592)	230.2	161.6	156.4	297.3	-9.2	290.4	285.5
VCrFe4.5Co2Ni1.5 [47]	3.542 (3.588)	239.5	161.3	165.3	308.0	-43.0	286.5	262.6
VCrFe4.5Co3Ni0.5 [47]	3.533 (3.590)	250.9	161.5	174.8	320.0	-87.8	279.9	229.8
VCrFe4.5Ni3.5 [47]	3.561	217.8	157.4	148.1	287.1	16.1	291.3	300.5
VCuFeCoNi [58]	3.592	215.9	166.6	132.2	265.6	38.5	280.3	300.0
Co2Cr1.25Fe0.75Ni0.75Mo0.25 [32]	3.555	276.7	186.3	173.3	332.0	-62.3	299.1	266.3
Co2.5Cr1.25Fe0.5Ni0.5Mo0.25 [32]	3.549	288.4	189.2	180.2	364.9	-87.8	320.3	274.6
Co1.5Cr1.25Fe1.0Ni1.0Mo0.25 [32]	3.566	272.7	190.7	166.9	318.0	-48.0	292.3	268.1

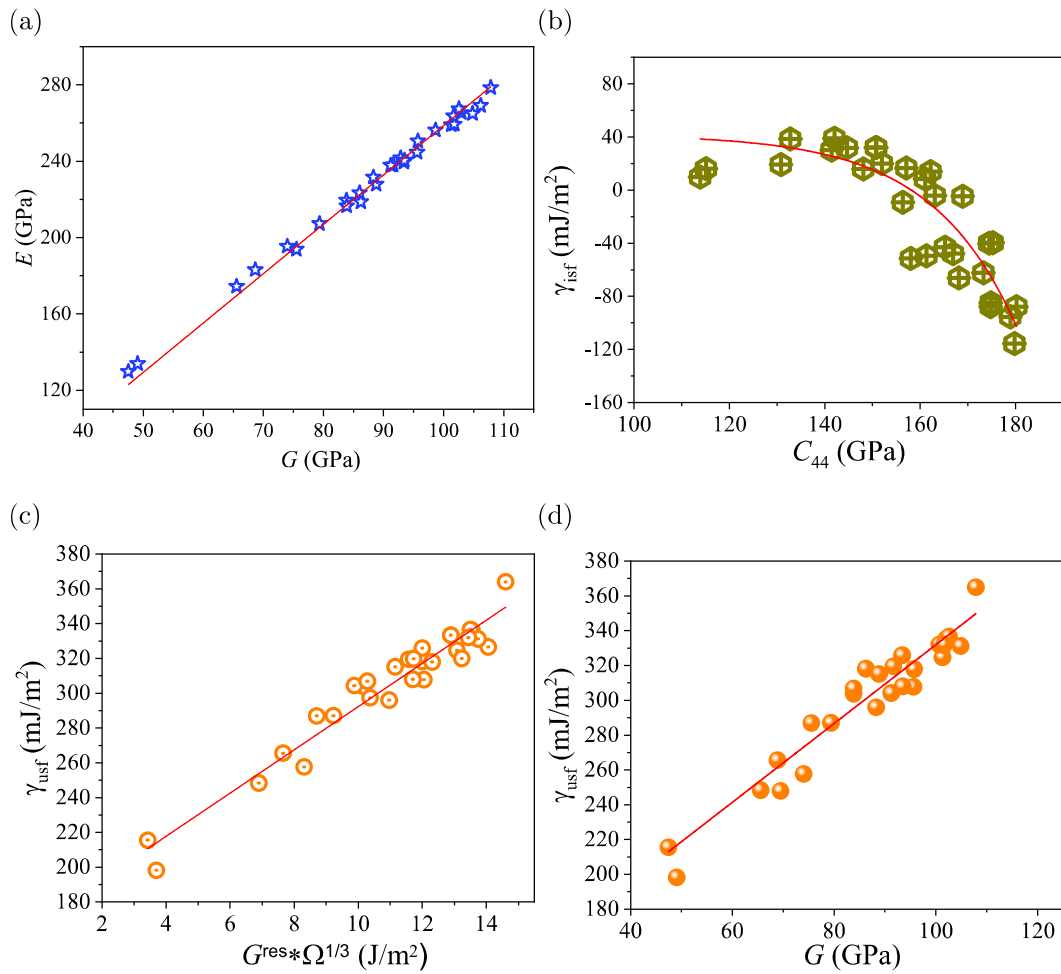


Fig. 2. Correlations between various calculated materials parameters for the present HEAs: (a) polycrystal Young's modulus E vs. shear G modulus, (b) ISFE γ_{isf} vs. shear elastic constant C_{44} , (c) USFE γ_{usf} vs. normalized, resolved shear modulus $G^{\text{res}}\Omega^{1/3}$, and (d) γ_{usf} vs. G . Lines are fits to the data points.

above. Since values of G can be reliably computed from values of E as discussed above (and vice versa), Young's modulus may serve as useful surrogate to estimate γ_{usf} in lack of G , with E being more easily accessible to experiments than G through tensile or compressive stress-strain lines, nano-indentation load-displacement curves, or ultrasound methods. Although the correlations displayed in Fig. 2(a) and (d) are valid for isotropic and homogeneous materials, they are expected to hold in materials with weak to moderate crystallographic texture.

To gain microscopic insights into tendencies for deformation twinning and transformation to hcp martensite in the present alloys, we illustrate in Fig. 1 the GSFE curves for various sequential slip paths leading to common stable planar defects: creation and annihilation of an ISF, formation of a twinning fault, and formation of a nano-hcp plate. These slip processes are commonly interpreted in terms of nucleation of leading (Burgers vector $b_{\text{lp}} = [11\bar{2}]/6$) and complementary trailing ($b_{\text{tp}} = [2\bar{1}\bar{1}]/6$) Shockley partials, in which the associated athermal nucleation barriers are obtained from the extrema of the GSFE curves (cf. Fig. 1):

- stacking fault (SF) mode, $\gamma(0 \leq x/b_p \leq 1)$: nucleation of b_{lp} with barrier γ_{usf} creates an isolated ISF.
- full slip (SL) mode, $\gamma_{\text{SL}}(1 \leq x/b_p \leq 2)$: nucleation of b_{tp} on the original slip plane with barrier $\gamma_{\text{usf}} - \gamma_{\text{isf}}$ removes the ISF and completes the full slip.
- twin (TW) mode, $\gamma_{\text{TW}}(1 \leq x/b_p \leq 2)$: a nanotwin fault forms due to nucleation of b_{lp} on the (111) slip plane adjacent to the original ISF with barrier $\gamma_{\text{utf}} - \gamma_{\text{isf}}$ (UTF: unstable twin fault).

- nano-hcp phase (NP) mode, $\gamma_{\text{NP}}(1 \leq x/b_p \leq 2)$: formation of a nano-hcp plate due to emission of b_{lp} on the next but one plane containing the original ISF with barrier $\gamma_{\text{upf}} - \gamma_{\text{isf}}$ (UPF: unstable phase fault).

The SL, TW, and NP modes are correlated modes as they require a pre-existing ISF. SF can be interpreted as formation of a two-layer hcp embryo, while NP describes the embryo's transverse thickening into a four-layer thin hcp plate; see stacking sequences in Fig. 1.

Two of the unstable planar defect energies were proposed to satisfy [61],

$$\gamma_{\text{utf}} - \gamma_{\text{isf}}/2 \simeq \gamma_{\text{usf}}, \quad (5)$$

which is readily seen to establish a relation between any two of the nucleation barriers for TW, SF, and SL modes. Here, we propose a second relation,

$$\gamma_{\text{upf}} - \gamma_{\text{isf}} \simeq \gamma_{\text{usf}}, \quad (6)$$

to measure how much the barrier for NP is altered by an pre-existing ISF. Introducing $\Lambda \equiv \gamma_{\text{isf}}/\gamma_{\text{usf}}$ as a characteristic material property as suggested previously [61], Fig. 3(a) and (b) establish that the ratios $\gamma_{\text{utf}}/\gamma_{\text{usf}}$ and $\gamma_{\text{upf}}/\gamma_{\text{usf}}$ in the present alloys scale closely, but not perfectly, with Λ according to two scaling relations readily deduced from Eqs. (5) and (6). Deviations from ideal scaling are more obvious for $\gamma_{\text{utf}}/\gamma_{\text{usf}}$ plausibly since the TW path involves faulting on the plane adjacent to an ISF and the NP path on the next but one. The scaling in Fig. 3(b) indicates that the resistance of an existing ISF to thicken by two (111) layers is slightly

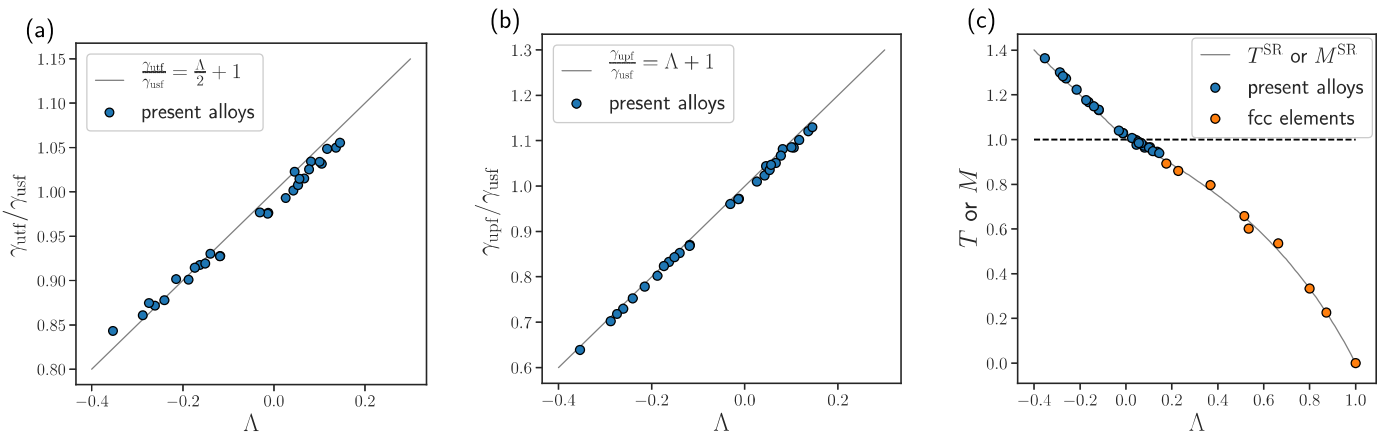


Fig. 3. Panels (a) and (b) show scaling plots of ratios of unstable planar fault energies as a function of the measure $\Lambda \equiv \gamma_{\text{isf}}/\gamma_{\text{usf}}$ and the solid lines indicate the scaling relations derived from Eqs. (5) and (6), respectively. Panel (c) shows the twinnability T for $\Lambda > 0$ and martensitability M for $\Lambda < 0$ as a function of Λ . The solid lines indicate T^{SR} and M^{SR} . The twinnability for fcc elements was derived from DFT data reported by Jin *et al.* [61].

lower (at most 6 mJ/m² for the present alloys) than that to create a new isolated ISF, suggesting that ISFs grow into hcp lamellae by repeated nucleation of b_{lp} . Generally, the scaling plots suggest short-ranged interactions between planar defects for sequential faulting on fcc {111} planes.

The competition between the SF, SL, TW, and NP modes on a specific {111} plane can be analyzed by comparing the projected components of an applied shear stress required to initiate slip in the respective slip directions. For the present purpose it suffices to recall that SF, TW, and NP have a common slip direction (b_{lp}) different from that of SL (b_{tp}). The competition between SF, TW, and NP is then determined by the lowest critical resolved shear stress, or equivalently, the lowest of the three associated energy barriers. Satisfaction of Eqs. (5) and (6) implies that, in the thermally nonactivated limit, (i) the TW mode can only be activated for $\gamma_{\text{isf}} > 0$ and competes with SL, (ii) the NP or SF mode can only be activated for $\gamma_{\text{isf}} < 0$ and competes with SL, (iii) the nucleation barriers for the TW, NP, and SF modes are equal for $\gamma_{\text{isf}} = 0$. Inspection of our calculated data (Table 1) shows that the present HEAs are largely congruent with this behavior. For all the HEAs with $\gamma_{\text{isf}} > 0$ ($\gamma_{\text{isf}} < 0$) the TW barrier is below (above) the NP barrier indeed. The SF barriers for two alloys with low, negative ISFE (CoCr2.5Fe2Mn0.5Ni4 and Co2Cr2.5FeMn0.5Ni4) are slightly larger than their TW barriers owing to a deviation from ideal scaling [Eq. (5)]. This does not imply that deformation twinning is predicted for these alloy cases, as the barriers for NP are below those of TW.

The competition between the two expected modes for positive ISFE, SL and TW, is commonly quantified by the twinning tendency or twinnability T [62,63], which may be expressed in terms of the respective nucleation barriers only [64,65],

$$T \equiv \frac{\gamma_{\text{usf}} - \gamma_{\text{isf}}}{\gamma_{\text{upf}} - \gamma_{\text{isf}}} \stackrel{\text{Eq.(5)}}{\approx} \frac{1 - \Lambda}{1 - \Lambda/2} \equiv T^{\text{SR}}. \quad (7)$$

T^{SR} approximates T closely for materials whose planar defect energies satisfy Eq. (5). Similarly, we introduce the tendency to form hcp martensite M , also referred to as martensitability, to rank the competition between SL and NP modes occurring for negative γ_{isf} as

$$M = \frac{\gamma_{\text{usf}} - \gamma_{\text{isf}}}{\gamma_{\text{upf}} - \gamma_{\text{isf}}} \stackrel{\text{Eq.(6)}}{\approx} 1 - \Lambda \equiv M^{\text{SR}}. \quad (8)$$

M^{SR} approximates M closely for materials whose planar defect energies satisfy Eq. (6).

Fig. 3(c) shows the calculated twinnabilities T and martensitabilities M versus Λ for the present HEAs. A higher value of T and a higher value of M suggest that deformation twinning and transformation to hcp martensite is more likely, respectively, whereas full slip is less likely.

Among the present HEAs, Co2CrCuFeMnNi has the highest T and VCrFe4.5Co3.5 has the highest M . For few of the 29 alloys, CoCrFeNi, CoCrFeMnNi, Co2Cr1.25Fe0.75Ni0.75Mo0.25, Co2.5Cr1.25Fe0.5-Ni0.5Mo0.25, and Co1.5Cr1.25Fe1.0Ni1.0Mo0.25, experimental information on primary deformation modes is available [32,40,66]. The experimental findings and results from the present theory are consistent in that fcc to hcp martensitic transformation occurs as a primary deformation mode in the fcc phase of CoCrFeNi, Co2Cr1.25Fe0.75-Ni0.75Mo0.25, Co2.5Cr1.25Fe0.5Ni0.5Mo0.25, and Co1.5Cr1.25-Fe1.0Ni1.0Mo0.25 [32,66]. For CoCrFeMnNi, we previously compared the predicted and observed deformation modes [40]. In essence, the experimental results indicated that deformation twinning is a primary mode of deformation in CoCrFeMnNi [32], in disagreement with the present theory predicting an fcc to hcp transformation.

Fig. 3(c) also shows that the calculated twinnabilities and martensitabilities lie close to the values resulting from satisfaction of the scaling relations (solid lines). To show that the common fcc elements follow the twinnability scaling up to $\Lambda = 1$, we included their T values, derived from previous DFT calculations of the GSFE surface [61], in plotting Fig. 3. The present HEAs with positive ISFEs have larger twinnabilities than Λ , which is the element with the largest value of T (0.89).

The predicted tendency to form martensite and twinning tendency may be verified by comparing the fraction of hcp-martensite and twin-related textures upon mechanical deformation. This deserves a comment in light of recent reports for Fe₅₀Mn₃₀Co₁₀Cr₁₀ and CrCrNi with supposedly near-zero ISFEs [67,68]. These two alloys host both the forward transformation from fcc to hcp-martensite as well as the reverse martensitic transformation from hcp to fcc. The fcc phase regions formed during the reverse deformation have a twin relation with the original fcc phase. The reverse transformation can obviously alter the fractions of hcp-martensite and twin-related textures, beyond to what is considered here for the plastic response of the fcc phases.

Finally, we recall that the present results are valid for statistically random solid solutions. CSRO (as a precursor for possible local chemical order on size scales of nm) may develop in HEAs, depending on thermomechanical processing, and influence dislocation dynamics, deformation microstructure, as well as macroscopic mechanical properties. Without performing dedicated calculations or experiments, it is, however, difficult to predict *a priori* whether the here considered multi-component solid solutions would contain CSRO and what kind of order would emerge. Further, plastic deformation is expected to diminish CSRO. Returning to the present GSFE and its interpretation in terms of partial dislocation slip, nucleation and glide of a first, leading partial in a domain exhibiting CSRO would locally reduce CSRO on the glide plane [69]. The CSRO is not restored by dislocations that glide in

succession on the same glide plane, and these dislocations now experience the energy barriers associated with the destroyed CSRO structure. Assuming that destruction of CSRO lowers the energy barriers that dislocations need to overcome, glide is then favoured on the original glide plane. This effect has been correlated with localised planar slip behaviour in solid solutions with well-developed CSRO, such Cu-Al and Cu-Zn [69,70] and CrCoNi [71].

4. Conclusions

The equilibrium lattice parameters, the elastic constants, and various stable and unstable planar defect energies of 29 fcc HEAs were calculated using first-principles calculations. Simple linear relations between the polycrystal Young's modulus and shear modulus and between the USFE and the resolved shear modulus and the polycrystal shear modulus were found. The calculated planar fault energies closely followed two scaling relations, suggesting that $\Lambda \equiv \gamma_{\text{isf}}/\gamma_{\text{usf}}$ is a characteristic measure in fcc materials. The tendencies to show deformation twinning or martensitic transformation to the hcp phase were analyzed based on the alloys' intrinsic energy barriers and predicted to rank with Λ , in which deformation twinning is predicted in the HEAs with positive γ_{isf} only and martensitic transformation in those with negative γ_{isf} . Λ may be considered as a useful design and selection parameter that can aid in tailoring microstructure mechanisms in fcc HEAs including transformation-induced plasticity and twinning-induced plasticity phenomena.

Data availability statement

The data that supports the findings of this study are available within the article.

Author statement

Xiaojie Li: Investigation, Data curation, Visualization. **Stephan Schönecker:** Supervision, Conceptualization, Methodology, Visualization, Writing-Reviewing and Editing. **Levente Vitos:** Discussion, Reviewing. **Xiaoqing Li:** Supervision, Conceptualization, Methodology, Writing-original draft, Project administration, Funding acquisition, Resources.

Declaration of competing interest

The authors declare that they have no known competing financial interests or personal relationships that could have appeared to influence the work reported in this paper.

Acknowledgments

The Swedish Research Council (grant agreement no. 2020-03736, 2017-06474, and 2019-04971), the Swedish Steel Producers' Association, the Swedish Foundation for Strategic Research, the Swedish Energy Agency (2017-006800), the Swedish Foundation for International Cooperation in Research and Higher Education (CH2020-8730) and the Hungarian Scientific Research Fund (research project OTKA 128229) are acknowledged for financial support. X.-Q. Li also gratefully acknowledges financial support from the Göran Gustafssons Stiftelse and the Carl Tryggers Stiftelse. The computations were performed on resources provided by the Swedish National Infrastructure for Computing (SNIC) at the National Supercomputer Centre in Linköping partially funded by the Swedish Research Council through grant agreement no. 2018-05973.

References

- [1] J.W. Yeh, S.K. Chen, S.J. Lin, J.Y. Gan, T.S. Chin, T.T. Shun, C.H. Tsau, S.Y. Chang, Nanostructured high-entropy alloys with multiple principal elements: novel alloy design concepts and outcomes, *Adv. Eng. Mater.* 6 (2004) 299–303.
- [2] B. Cantor, I.T.H. Chang, P. Knight, A.J.B. Vincent, Microstructural development in equiatomic multicomponent alloys, *Mater. Sci. Eng. A* 375 (2004) 213–218.
- [3] Z. Li, D. Raabe, Strong and ductile non-equiatomic high-entropy alloys: design, processing, microstructure, and mechanical properties, *JOM* 21 (2017) 1–8.
- [4] S. Allain, J.-P. Chateau, O. Bouaziz, S. Migot, N. Guelton, Correlations between the calculated stacking fault energy and the plasticity mechanisms in Fe-Mn-C alloys, *Mater. Sci. Eng., A* 387–389 (2004) 158–162, <https://doi.org/10.1016/j.msea.2004.01.059>, 13th International Conference on the Strength of Materials, <http://www.sciencedirect.com/science/article/pii/S0921509304004356>.
- [5] B.C. De Cooman, Y. Estrin, S.K. Kim, Twinning-induced plasticity (TWIP) steels, *Acta Mater.* 142 (2018) 283–362, <https://doi.org/10.1016/j.actamat.2017.06.046>, <http://www.sciencedirect.com/science/article/pii/S135964517305219>.
- [6] W.G. Ahlborn H, Einfluss von Verformungsgrad und Temperatur auf die Textur von Silberdrähten, *Z. Metallk.* 54 (1963) 1–6.
- [7] A. English, G. Chin, On the variation of wire texture with stacking fault energy in f.c.c. metals and alloys, *Acta Metall.* 13 (9) (1965) 1013–1016, [https://doi.org/10.1016/0001-6160\(65\)90010-6](https://doi.org/10.1016/0001-6160(65)90010-6).
- [8] M.A. Fortes, B. Ralph, Deformation twinning and double twinning in iridium, *J. Less Common Met.* 22 (2) (1970) 201–208, [https://doi.org/10.1016/0022-5088\(70\)90020-2](https://doi.org/10.1016/0022-5088(70)90020-2).
- [9] R. Adamsku, S. Grebenkin, A. Yermakov, P. Panfilov, On mechanical twinning in iridium under compression at room temperature, *J. Mater. Sci. Lett.* 13 (1994) 865–867, <https://doi.org/10.1007/BF00273232>.
- [10] J.P. Hirth, J. Lothe, *Theory of Dislocations*, second ed., Wiley, New York, 1982.
- [11] S. Crampin, K. Hampel, D.D. Vvedensky, J.M. MacLaren, The calculation of stacking fault energies in close-packed metals, *J. Mater. Res.* 5 (10) (1990) 2107–2119, <https://doi.org/10.1557/JMR.1990.2107>.
- [12] V. Vitek, Intrinsic stacking faults in body-centred cubic crystals, *Phil. Mag. A* 18 (154) (1968) 773–786, <https://doi.org/10.1080/14786436808227500>, doi: 10.1080/14786436808227500.
- [13] J.R. Rice, Dislocation nucleation from a crack tip: an analysis based on the Peierls concept, *J. Mech. Phys. Solid.* 40 (2) (1992) 239–271, [https://doi.org/10.1016/S0022-5096\(05\)80012-2](https://doi.org/10.1016/S0022-5096(05)80012-2), <http://www.sciencedirect.com/science/article/pii/S0022509605800122>.
- [14] B. Li, B. Cao, K. Ramesh, E. Ma, A nucleation mechanism of deformation twins in pure aluminum, *Acta Mater.* 57 (2009) 4500–4507.
- [15] A.G. Froseth, H.V. Swygenhoven, P.M.I. Derlet, The influence of twins on the mechanical properties of nc-Al, *Acta Mater.* 52 (2004) 2259–2268.
- [16] H.V. Swygenhoven, P.M.I. Derlet, A.G. Frøseth, Stacking fault energies and slip in nanocrystalline metals, *Nat. Mater.* 3 (2004) 399–403.
- [17] V. Yamakov, D. Wolf, S.R. Phillpot, A.K. Mukherjee, H. Gleiter, Deformation-mechanism map for nanocrystalline metals by molecular-dynamics simulation, *Nat. Mater.* 3 (2004) 43–47.
- [18] P. Kwasniak, H. Garbacz, K. Kurzydłowski, Solid solution strengthening of hexagonal titanium alloys: restoring forces and stacking faults calculated from first principles, *Acta Mater.* 102 (2016) 304–314.
- [19] S. Ogata, Ideal pure shear strength of aluminum and copper, *Science* 298 (5594) (2002) 807–811.
- [20] X. Sun, S. Lu, R. Xie, X. An, W. Li, T. Zhang, C. Liang, X. Ding, Y. Wang, H. Zhang, L. Vitos, Can experiment determine the stacking fault energy of metastable alloys? *Mater. Des.* 199 (2021), 109396 <https://doi.org/10.1016/j.matdes.2020.109396>, <https://www.sciencedirect.com/science/article/pii/S0264127520309321>.
- [21] K.V. Werner, F. Niessen, M. Villa, M.A.J. Somers, Experimental validation of negative stacking fault energies in metastable face-centered cubic materials, *Appl. Phys. Lett.* 119 (14) (2021), 141902, <https://doi.org/10.1063/5.0063761>, doi: 10.1063/5.0063761.
- [22] K. Ishida, Direct estimation of stacking fault energy by thermodynamic analysis, *Phys. Status Solidi A* 36 (1976) 717–728.
- [23] P. Hohenberg, W. Kohn, Inhomogeneous electron gas, *Phys. Rev.* 136 (1964) B864–B871.
- [24] J.P. Perdew, K. Burke, M. Ernzerhof, Generalized gradient approximation made simple, *Phys. Rev. Lett.* 77 (1996) 3865–3868.
- [25] W. Kohn, L.J. Sham, Self-consistent equations including exchange and correlation effects, *Phys. Rev.* 140 (1965), A1133.
- [26] O.K. Andersen, O. Jepsen, G. Krier, V. Kumar, O.K. Andersen, A. Mookerjee (Eds.), *Lectures on Methods of Electronic Structure Calculations*, World Scientific, Singapore, 1994, p. 63.
- [27] L. Vitos, Total-energy method based on the exact muffin-tin orbitals theory, *Phys. Rev. B* 64 (2001), 014107.
- [28] B.L. Gyorffy, Coherent-potential approximation for a nonoverlapping-muffin-tin-potential model of random substitutional alloys, *Phys. Rev. B* 5 (1972) 2382–2384.
- [29] L. Vitos, *Computational Quantum Mechanics for Materials Engineers*, Springer-Verlag, London, 2007.
- [30] B.L. Gyorffy, A.J. Pindor, J. Staunton, G.M. Stocks, H. Winter, A first-principles theory of ferromagnetic phase transitions in metals, *J. Phys. F Met. Phys.* 15 (1985) 1337–1386.
- [31] B. Wasilewski, W. Marciniański, M. Werwiński, Curie temperature study of Y_{(Fe_{1-x}Co_x)₂} and Zr(Fe_{1-x}Co_x)₂ systems using mean field theory and Monte Carlo method, *J. Phys. D Appl. Phys.* 51 (17) (2018), 175001.

- [32] D. Wei, X. Li, S. Schönecker, J. Jiang, W.M. Choi, B.J. Lee, H.S. Kim, A. Chiba, H. Kato, Development of strong and ductile metastable face-centered cubic single-phase high-entropy alloys, *Acta Mater.* 181 (2019) 318–330.
- [33] X. Wang, Y. Zhang, Y. Qiao, G. Chen, Novel microstructure and properties of multicomponent CoCrCuFeNiTix alloys, *Intermetallics* 15 (3) (2007) 357–362, <https://doi.org/10.1016/j.intermet.2006.08.005>, <http://www.sciencedirect.com/science/article/pii/S0966979506002457>.
- [34] B. Gludovatz, A. Hohenwarter, D. Cattoor, E.H. Chang, E.P. George, R.O. Ritchie, A fracture-resistant high-entropy alloy for cryogenic applications, *Science* 345 (6201) (2014) 1153–1158.
- [35] A. Zaddach, C. Niu, A. Oni, M. Fan, J. LeBeau, D. Irving, C. Koch, Structure and magnetic properties of a multi-principal element NiFeCrCoZnMn alloy, *Intermetallics* 68 (2016) 107–112, <https://doi.org/10.1016/j.intermet.2015.09.009>.
- [36] M.S. Lucas, L. Mauger, J.A. Muñoz, Y. Xiao, A.O. Sheets, S.L. Semiatin, J. Horwath, Z. Turgut, Magnetic and vibrational properties of high-entropy alloys, *J. Appl. Phys.* 109 (7) (2011), 07E307.
- [37] M.S. Lucas, D. Belyea, C. Bauer, N. Bryant, E. Michel, Z. Turgut, S.O. Leontsev, J. Horwath, S.L. Semiatin, M.E. McHenry, C.W. Miller, Thermomagnetic analysis of FeCoCrNi alloys: magnetic entropy of high-entropy alloys, *J. Appl. Phys.* 113 (17) (2013), 17A923.
- [38] Y.F. Kao, S.K. Chen, T.J. Chen, P.C. Chu, J.W. Yeh, S.J. Lin, Electrical, magnetic, and hall properties of Al_xCoCrFeNi high-entropy alloys, *J. Alloys Compd.* 509 (5) (2011) 1607–1614.
- [39] S. Kibey, J. Liu, D. Johnson, H. Sehitoglu, Predicting twinning stress in fcc metals: linking twin-energy pathways to twin nucleation, *Acta Mater.* 55 (2007) 6843–6851.
- [40] S. Schönecker, W. Li, L. Vitos, X. Li, Effect of strain on generalized stacking fault energies and plastic deformation modes in fcc-hcp polymorphic high-entropy alloys: a first-principles investigation, *Phys. Rev. Mater.* 5 (2021), 075004.
- [41] R. Hill, The elastic behaviour of a crystalline aggregate, *Proc. Phys. Soc. A* 65 (1952) 349–354.
- [42] V.L. Moruzzi, J.F. Janak, K. Schwarz, Calculated thermal properties of metals, *Phys. Rev. B* 37 (1988) 790–799, <https://doi.org/10.1103/PhysRevB.37.790>.
- [43] Z. Pei, B. Dutta, F. Körmann, M. Chen, Hidden effects of negative stacking fault energies in complex concentrated alloys, *Phys. Rev. Lett.* 126 (2021) 255502, <https://doi.org/10.1103/PhysRevLett.126.255502>.
- [44] D. Ma, B. Grabowski, F. Körmann, B. Neugebauer, D. Raabe, Ab initio thermodynamics of the CoCrFeMnNi high entropy alloy: importance of entropy contributions beyond the configurational one, *Acta Mater.* 100 (2015) 90–97.
- [45] A.J. Zaddach, C. Niu, C.C. Koch, D.L. Irving, Mechanical properties and stacking fault energies of NiFeCrCoMn high-entropy alloy, *JOM* 65 (2013) 1780–1789.
- [46] W. Choi, Y. Jo, S. Sohn, S. Lee, B. Lee, Understanding the physical metallurgy of the CoCrFeMnNi high-entropy alloy: an atomistic simulation study, *npj Comput. Mater.* 4 (1). doi:10.1038/s41524-017-0060-9.
- [47] Y.H. Jo, W.M. Choi, D.G. Kim, A. Zargaran, S.S. Sohn, H.S. Kim, B.J. Lee, N.J. Kim, S.L. S, FCC to BCC transformation-induced plasticity based on thermodynamic phase stability in novel V10Cr10Fe45CoxNi35-x medium-entropy alloys, *Sci. Rep.* 9 (1) (2019) 2948.
- [48] A. Gali, E. George, Tensile properties of high- and medium-entropy alloys, *Intermetallics* 39 (2013) 74–78, <https://doi.org/10.1016/j.intermet.2013.03.018>, <http://www.sciencedirect.com/science/article/pii/S0966979513000903>.
- [49] Z. Wu, H. Bei, F. Otto, G. Pharr, E. George, Recovery, recrystallization, grain growth and phase stability of a family of FCC-structured multi-component equiatomic solid solution alloys, *Intermetallics* 46 (2014) 131–140, <https://doi.org/10.1016/j.intermet.2013.10.024>.
- [50] R.-F. Zhao, B. Ren, G.-P. Zhang, Z.-X. Liu, J. Jian Zhang, Effect of Co content on the phase transition and magnetic properties of Co_xCrCuFeMnNi high-entropy alloy powders, *J. Magn. Magn. Mater.* 468 (2018) 14–24, <https://doi.org/10.1016/j.jmmm.2018.07.072>.
- [51] R. Chang, W. Fang, X. Bai, C. Xia, X. Zhang, H. Yu, B. Liu, F. Yin, Effects of tungsten additions on the microstructure and mechanical properties of CoCrNi medium entropy alloys, *J. Alloys Compd.* 790 (2019) 732–743, <https://doi.org/10.1016/j.jallcom.2019.03.235>.
- [52] B. Ren, Z. Liu, D. Li, L. Shi, B. Cai, M. Wang, Effect of elemental interaction on microstructure of CuCrFeNiMn high entropy alloy system, *J. Alloys Compd.* 493 (1) (2010) 148–153, <https://doi.org/10.1016/j.jallcom.2009.12.183>.
- [53] C. Li, J. Li, M. Zhao, Q. Jiang, Effect of alloying elements on microstructure and properties of multiprincipal elements high-entropy alloys, *J. Alloys Compd.* 475 (1) (2009) 752–757, <https://doi.org/10.1016/j.jallcom.2008.07.124>.
- [54] Q. Ding, Y. Zhang, X. Chen, X. Fu, D. Chen, S. Chen, L. Gu, F. Wei, H. Bei, Y. Gao, M. Wen, J. Li, Z. Zhang, T. Zhu, R. Ritchie, Q. Yu, Tuning element distribution, structure and properties by composition in high-entropy alloys, *Nature* 574 (2019) 223–227.
- [55] W.-M. Choi, Y.H. Jo, D.G. Kim, S.S. Sohn, S. Lee, B.-J. Lee, A thermodynamic description of the Co-Cr-Fe-Ni-V system for high-entropy alloy design, *Calphad* 66 (2019), 101624, <https://doi.org/10.1016/j.calphad.2019.05.001>.
- [56] C.-M. Lin, H.-L. Tsai, Equilibrium phase of high-entropy FeCoNiCrCu0.5 alloy at elevated temperature, *J. Alloys Compd.* 489 (1) (2010) 30–35, <https://doi.org/10.1016/j.jallcom.2009.09.041>.
- [57] W. Liu, Z. Lu, J. He, J. Luan, Z. Wang, B. Liu, Y. Liu, M. Chen, C. Liu, Ductile CoCrFeNiMox high entropy alloys strengthened by hard intermetallic phases, *Acta Mater.* 116 (2016) 332–342, <https://doi.org/10.1016/j.actamat.2016.06.063>.
- [58] Y. Zhang, Y. Zhou, J. Lin, G. Chen, P. Liaw, Solid-solution phase formation rules for multi-component alloys, *Adv. Eng. Mater.* 10 (6) (2008) 534–538, <https://doi.org/10.1002/adem.200700240>, arXiv:<https://www.onlinelibrary.wiley.com/doi/pdf/10.1002/adem.200700240>.
- [59] J.F. Nye, *Physical Properties of Crystals: Their Representation by Tensors and Matrices*, Oxford University Press, New York, 1960.
- [60] H.M. Ledbetter, Ratio of the shear and Young's moduli for polycrystalline metallic elements, *Mater. Sci. Eng.* 27 (1977) 133–136.
- [61] Z.H. Jin, S.T. Dunham, H. Gleiter, H. Hahn, P. Gumbsch, A universal scaling of planar fault energy barriers in face-centered cubic metals, *Scripta Mater.* 64 (2011) 605–608.
- [62] E.B. Tadmor, N. Bernstein, A first-principles measure for the twinnability of FCC metals, *J. Mech. Phys. Solid.* 52 (11) (2004) 2507–2519, <https://doi.org/10.1016/j.jmps.2004.05.002>.
- [63] R. Asaro, S. Suresh, Mechanistic models for the activation volume and rate sensitivity in metals with nanocrystalline grains and nano-scale twins, *Acta Mater.* 53 (2005) 3369–3382.
- [64] D.H. Warner, W.A. Curtin, S. Qu, Rate dependence of crack-tip processes predicts twinning trends in f.c.c. metals, *Nat. Mater.* 6 (2007) 876–881.
- [65] B.Q. Li, M.L. Sui, S.X. Mao, Twinnability prediction for fcc metals, *J. Mater. Sci. Technol.* 27 (2) (2011) 97.
- [66] Q. Lin, J. Liu, X. An, H. Wang, Y. Zhang, X. Liao, Cryogenic-deformation-induced phase transformation in an FeCoCrNi high-entropy alloy, *Mater. Res. Lett.* 6 (4) (2018) 236–243.
- [67] W. Lu, C. Liebscher, G. Dehm, D. Raabe, Z. Li, Bidirectional transformation enables hierarchical nanolaminate dual-phase high-entropy alloys, *Adv. Mater.* 30–44 (2018), e1804727.
- [68] Y. Chen, D. Chen, X. An, Y. Zhang, Z. Zhou, S. Lu, P. Munroe, S. Zhang, X. Liao, T. Zhu, Z. Xie, Unraveling dual phase transformations in a CrCoNi medium-entropy alloy, *Acta Mater.* 215 (2021), 117112, <https://doi.org/10.1016/j.actamat.2021.117112>, <https://www.sciencedirect.com/science/article/pii/S1359645421004924>.
- [69] V. Gerold, H. Karthaler, On the origin of planar slip in f.c.c. alloys, *Acta Metall.* 37 (8) (1989) 2177–2183, [https://doi.org/10.1016/0001-6160\(89\)90143-0](https://doi.org/10.1016/0001-6160(89)90143-0).
- [70] R. Niu, X. An, L. Li, Z. Zhang, Y.-W. Mai, X. Liao, Mechanical properties and deformation behaviours of submicron-sized Cu-Al single crystals, *Acta Mater.* 223 (2022), 117460, <https://doi.org/10.1016/j.actamat.2021.117460>.
- [71] R. Zhang, S. Zhao, J. Ding, Y. Chong, T. Jia, C. Ophus, M. Asta, R.O. Ritchie, A. M. Minor, Short-range order and its impact on the CrCoNi medium-entropy alloy, *Nature* 581 (2020) 283–287.